



HAL
open science

Low-Complexity 3D InSAR Imaging Using a Compressive Hardware Device and a Single Receiver

Mor Diamo Lo, Matthieu Davy, Laurent Ferro-Famil

► **To cite this version:**

Mor Diamo Lo, Matthieu Davy, Laurent Ferro-Famil. Low-Complexity 3D InSAR Imaging Using a Compressive Hardware Device and a Single Receiver. *Sensors*, 2022, 22 (15), pp.5870. 10.3390/s22155870 . hal-03771179

HAL Id: hal-03771179

<https://hal.science/hal-03771179>

Submitted on 7 Sep 2022

HAL is a multi-disciplinary open access archive for the deposit and dissemination of scientific research documents, whether they are published or not. The documents may come from teaching and research institutions in France or abroad, or from public or private research centers.

L'archive ouverte pluridisciplinaire **HAL**, est destinée au dépôt et à la diffusion de documents scientifiques de niveau recherche, publiés ou non, émanant des établissements d'enseignement et de recherche français ou étrangers, des laboratoires publics ou privés.



Distributed under a Creative Commons Attribution 4.0 International License

Article

Low-Complexity 3D InISAR Imaging Using a Compressive Hardware Device and a Single Receiver

Mor Diama Lo ^{1,*}, Matthieu Davy ¹ and Laurent Ferro-Famil ^{2,3}¹ IETR, University of Rennes 1, 35000 Rennes, France² ISAE-SUPAERO, University of Toulouse, 31055 Toulouse, France³ CESBIO, University of Toulouse, CNES/CNRS/INRAE/IRD/UPS, 31401 Toulouse, France

* Correspondence: mor-diama.lo@univ-rennes1.fr; Tel.: +33-2-2323-6720

Abstract: An Interferometric Inverse SAR system is able to perform 3D imaging of non-cooperative targets by measuring their responses over time and through several receiving antennas. Phase differences between signals acquired with a spatial diversity in vertical or horizontal directions are used to localize moving scatterers in 3D. The use of several receiving channels generally results into a costly and complex hardware solution, and this paper proposes performing this multichannel acquisition using a single receiver and a hardware compressive device, based on a chaotic cavity which simultaneously multiplexes in the spectral domain signals acquired over different antennas. The radar responses of the scene are encoded in the spectral domain onto the single output of a leaky chaotic cavity, and can be retrieved by solving an inverse problem involving the random transfer matrix of the cavity. The applicability of this compressed sensing approach for the 3D imaging of a non-cooperative target using low-complexity hardware is demonstrated using both simulations and measurements. This study opens up new perspectives to reduce the hardware complexity of high-resolution ISAR systems.

Keywords: ISAR; interferometric ISAR; radar; compressive device; computational imaging

**Citation:** Lo, M.D.; Davy, M.;Ferro-Famil, L. Low-Complexity 3D InISAR Imaging Using a Compressive Hardware Device and a Single Receiver. *Sensors* **2022**, *22*, 5870. <https://doi.org/10.3390/s22155870>

Academic Editor: Renato Machado

Received: 24 June 2022

Accepted: 2 August 2022

Published: 5 August 2022

Publisher's Note: MDPI stays neutral with regard to jurisdictional claims in published maps and institutional affiliations.



Copyright: © 2022 by the authors. Licensee MDPI, Basel, Switzerland. This article is an open access article distributed under the terms and conditions of the Creative Commons Attribution (CC BY) license (<https://creativecommons.org/licenses/by/4.0/>).

1. Introduction

Inverse Synthetic Aperture Radar (ISAR) is a technique used for many applications related to target classification and recognition, due to its ability to provide high-resolution images of a scene. In its simplest form, two-dimensional (2D) ISAR imaging may be associated with the filtered projection of three-dimensional target reflectivity onto the Image Projection Plane (IPP) [1,2]. These images are generated by estimating the typically unknown motion of the target relative to the observing the radar [1,3] or using specific properties of the radar responses of artificial objects [4]. The interpretation of 2D conventional ISAR images is, however, difficult most of the time [1,2,5], and three-dimensional ISAR images with detailed geometric feature of the scatterers, such as their lengths, widths and heights, are necessary for target recognition and classification [5].

Several techniques have been proposed to form 3D ISAR images. Firstly, a time-domain technique approach [6,7] using a single sensor based on 3D matched filtering [8,9] for 3D reconstruction of non-cooperative targets. This approach, which uses a sequence of ISAR images [10–13], requires a long observation time and accurate scattering point extraction and scattering point trace matrix decomposition. The corresponding algorithm, therefore, has considerable computational complexity. Another approach is based on interferometric principles and makes use of multiple receivers [14–17]. This spatial diversity provides height information which makes it possible to separate scatterers with the same range–Doppler values. More generally, 3D-ISAR interferometric images are formed using a two-dimensional antenna array. In [5,18], a L-shaped array configuration was proposed to estimate the height of the target main scattering centers from the joint phases difference

between ISAR images computed at different antenna locations. This technique can be implemented with a short observation time, without the need for a scatterer tracking algorithm. However, its accuracy depends on the relative distance between the target dimensions and receiver baselines. 3D InSAR was demonstrated experimentally for both complex land [19] and maritime targets [20,21]. Finally, the last approach relies on a 3D bistatic ISAR imaging technique to estimate scattering centers in 3D cartesian space [22,23].

In interferometric approaches, the signals must, however, be recorded on a synchronized antenna array which increases the price and complexity of the system. Here, we combine 3D Interferometry Inverse Synthetic Aperture Radar and computational imaging to obtain 3D images of a scene from a single receiving channel. The principle of computational imaging techniques in the microwave range is to connect the array of receiving antennas to a dispersive component with a high quality (Q) factor and encode the signals onto a single spectrum. The reverberation within the component provides a space/frequency transfer matrix between the inputs and the output signals, which is random given that the spacing between two frequencies is larger than the spectral correlation length of the device [24,25]. The spectral correlation length is typically equal to $1/\tau$, where τ is the temporal decay factor of transmitted signals. Using that, the random transfer functions of the cavity are nearly orthogonal; the incoming signals can be reconstructed numerically by solving an inverse problem with deconvolution techniques such as an adaptive filter or matrix inversion [26]. This technique has the advantage of using a cheap component such as a photonic crystal [27], a multiple scattering medium [28,29] or a chaotic cavity [24,25,30–33].

In this article, we demonstrate numerically and experimentally that InSAR techniques can be combined with the use of chaotic cavity as a compressive sensing device to obtain high-resolution 3D images of a moving target. This paper is organized as follows: we first present the compressive sensing device and our methodology to solve the inverse problem in Section 2. After detailing the geometry of the InSAR system in Section 3 and the InSAR algorithm in Section 4, the Sections 5 and 6 are devoted to numerical simulations and experimental results validating our approach.

2. Compressive Sensing Device

2.1. Device Description

A N to 1 passive multiplexer, operating over a frequency band centered around $f_0 = 6$ GHz, and consisting of a metallic chaotic cavity manufactured at the IETR, can be seen in Figure 1). The cavity has a volume of 0.075 m^3 and its dimensions, $50 \text{ cm} \times 50 \text{ cm} \times 30 \text{ cm}$, are all much larger than the carrier signal wavelength. The cavity is made fully chaotic by placing three metallic hemispheres on the walls, as well as a deformed corner, shown in Figure 1. Four coaxial to waveguide transitions are connected to the cavity through a wall in order to multiplex $N = 3$ input signals, $s_n(\tau)$ with $n = 1, 2$ or 3 , into a composite compressed signal $y(\tau)$, accessible at a fourth port on the wall, and measured in the spectral domain by a Vector Network Analyzer (VNA). Multiple scattering of waves occurring within this enclosure provides large spectral diversity that may be used to retrieve the input signals, $s_n(\tau)$ using the measured scalar information, $y(\tau)$, and the known chaotic impulse responses, $s_n(\tau)$, relating the inputs of the cavity to its output. The quality of the reconstruction is conditioned the number of degrees of freedom, or independent components that may be addressed over the measured spectral domain, given by [24,25]

$$N_f = B\tau_r \quad (1)$$

where τ_r is the typical reverberation time of the cavity, i.e., the spread of its impulse response, approximately equal to 80 ns with the considered device, and B is the width of the measured spectral domain, equal to 2 GHz in this experiment. The configuration adopted in this work yields a high quality factor $Q = 2\pi f_0 \tau_r \approx 3000$ [24]. This leads to a minimum number of frequencies to code the information on all modes of the box $N_f \geq 1600$. Hence, we choose $N_f = 2001$ spectral coordinates for a characterization of the

transfer functions of the box. The cross-correlation between the impulse responses of ports p and q is formulated as

$$\rho_{pq}(\tau) = c_p(\tau) \otimes c_q^*(-\tau) \quad (2)$$

with \otimes as the convolution operator, and where the individual impulse responses are normalized so that $\rho_{pp}(0) = 1, \forall p$. The amplitude of the correlation functions $|\rho_{11}|$ and $|\rho_{12}|$, displayed in Figure 2a, shows a small degree of correlation between these two transfer functions and a rather narrow auto-correlation pattern. The orthogonality of the system transfer functions can be generally observed by calculating the matrix of transmission coefficients c_{pq} in the frequency domain as

$$c_{pq} = \sum_{j=1}^{N_f} |c_p(f_j)c_q^*(f_j)| / N_f \quad (3)$$

The matrix of correlation coefficients between the three transfer functions is close to diagonal, as shown in Figure 2b. A completely diagonal matrix would provide perfect reconstruction of incoming signals. However, the quality of the reconstruction of the inputs waveform is limited due to the finite value of N_f .

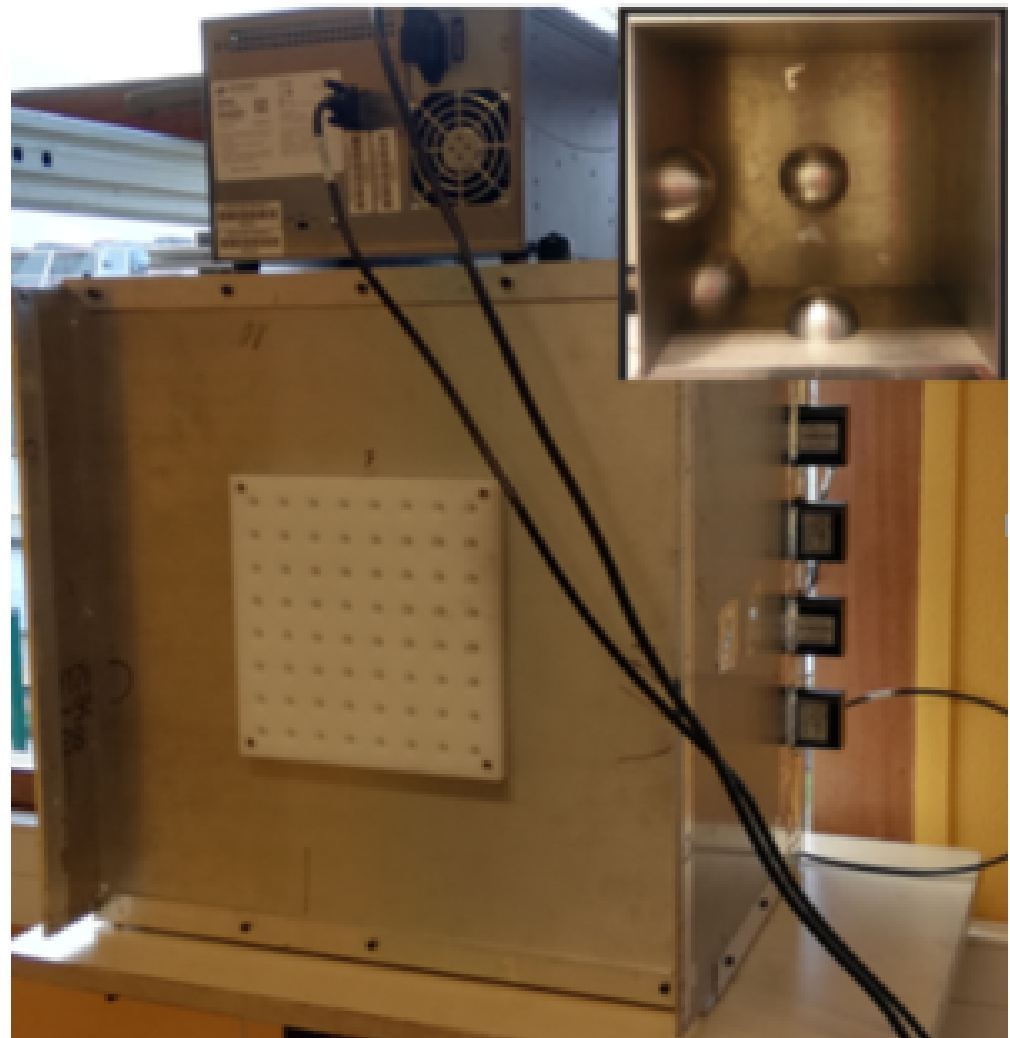


Figure 1. Photograph of the chaotic cavity. Four ports can be seen on the right hand wall of the cavity. The interior of the cavity, containing four hemispheres, is shown in the inset.

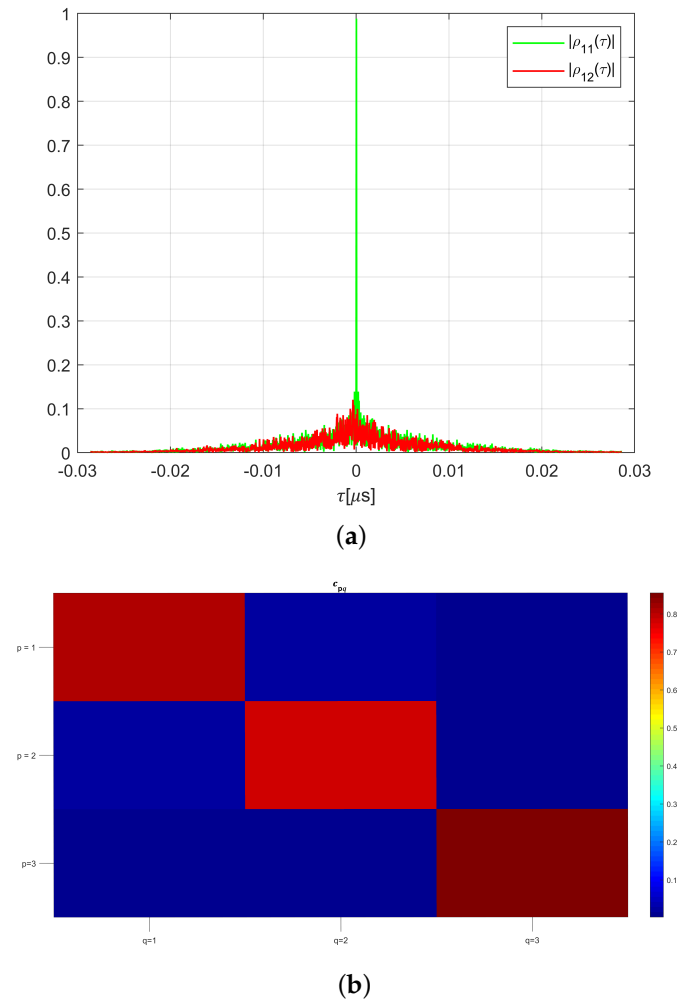


Figure 2. Features of the transfer functions of the chaotic cavity. **(a)** Amplitude of time—domain correlation functions (2); **(b)** Spectral transmission coefficients (3).

2.2. Vector Signal Retrieval Principle

As illustrated in Figure 3, the output time-domain signal recorded for a $N \times 1$ passive coding device may be written as

$$\mathbf{y}(\tau) = \sum_{n=1}^N \mathbf{c}_n(\tau) \otimes s_n(\tau) + v(\tau), \quad (4)$$

where $v(\tau)$ stands for the acquisition noise. In the spectral domain, (4) simplifies to

$$\mathbf{y} = \sum_{n=1}^N \mathbf{c}_n \odot \mathbf{s}_n + \mathbf{v}, \quad (5)$$

where \odot represents the elements-wise product, and \mathbf{y} is defined as $\mathbf{y} = [y(f_1), \dots, y(f_M)]^T$ where $y(f)$ stands for the Fourier transform of $y(\tau)$, and f_1, \dots, f_M represent spectral coordinates at which the received signal is measured. The expression of the measured signal in (5) may be represented using a linear transformation

$$\mathbf{y} = \mathbf{C} \mathbf{s} + \mathbf{v}, \quad (6)$$

with $\mathbf{C} = [\mathbf{C}_1, \dots, \mathbf{C}_N] \in \mathbb{C}^{M \times MN}$, the cavity channel transfer matrix, $\mathbf{C}_n = \text{diag}(c_n) \in \mathbb{C}^{M \times M}$, the transfer matrix of a single channel, and $\mathbf{s} = [s_1^T, \dots, s_N^T]^T \in \mathbb{C}^{MN}$, the input vector signal.

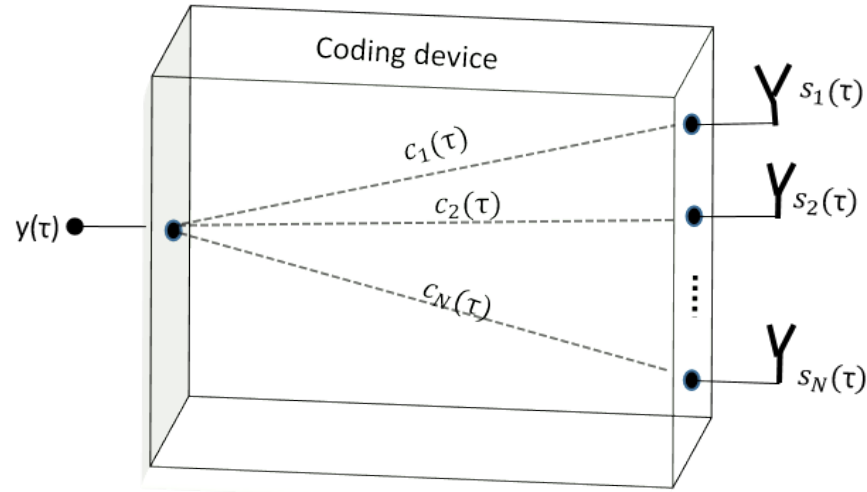


Figure 3. Synopsis of the hardware compressive coding device used in this study.

Among the the wide variety of inversion approaches which could be applied to retrieve \mathbf{s} from \mathbf{y} , quadratically regularized Linear Least Squares Estimation techniques are particularly interesting, as they can be implemented in the form of a linear transformation, and related to physical interpretations. The corresponding criterion to be minimized is given by

$$J(\mathbf{s}) = \|\mathbf{y} - \mathbf{C}\mathbf{s}\|^2 + \lambda \|\mathbf{\Gamma}\mathbf{s}\|^2 \quad (7)$$

whose solution is $\hat{\mathbf{s}} = \mathbf{Q}\mathbf{y}$ with

$$\mathbf{Q} = (\mathbf{C}^H\mathbf{C} + \lambda\mathbf{\Gamma}^H\mathbf{\Gamma})^{-1}\mathbf{C}^H \quad (8)$$

where λ is a user-defined regularization weight and $\mathbf{\Gamma}$ is an arbitrary matrix, whose structure may be used to confer specific properties to the estimated signal. In particular, $\lambda = 0$ corresponds to the non-regularized LLSE, whereas $\lambda > 0$ leads to the so-called Tikhonov regularization, known to improve the conditioning of the inverse problem, which operates uniformly over the signal space if $\mathbf{\Gamma}^H\mathbf{\Gamma} = \mathbf{I}$. For large λ values, and $\mathbf{\Gamma}^H\mathbf{\Gamma} = \mathbf{I}$ the inversion approach is equivalent to the matched filter solution, with $\mathbf{Q} \propto \mathbf{C}^H$, whose features may be appreciated from the cross-correlation plots given in Figure 2, and which provides optimal signal-to-noise ratio characteristics after reconstruction.

3. Geometry and Signal Model

The InSAR system used in this study consists of a transmitting antenna (\mathbf{P}_T), three receiving antennas ($\mathbf{P}_{RC}, \mathbf{P}_{RH}, \mathbf{P}_{RV}$) and a chaotic box. The receiving antennas lie on both a horizontal and a vertical baseline with a L-shape configuration, as originally proposed in [5,18]. The receiving channels are connected to the inputs ports of the coding device and a single output signal is measured. The radar system is pointed at the scene with a vertical orientation β and a horizontal orientation α . The corresponding squint mode induces a geometrical distortion [34] of the synthesized InSAR images.

The InSAR geometry is represented in Figure 4. The reference system $T_0 = \{\hat{X}, \hat{Y}, \hat{Z}\}$ is expressed at the radar antenna array, whereas the reference system $T_1 = \{X, Y, Z\}$ is centred on the centre of rotation of the target at $t = 0$. The axis \hat{Y} defines the ground range, while \hat{X} and \hat{Z} correspond to the horizontal and vertical baseline directions, respectively.

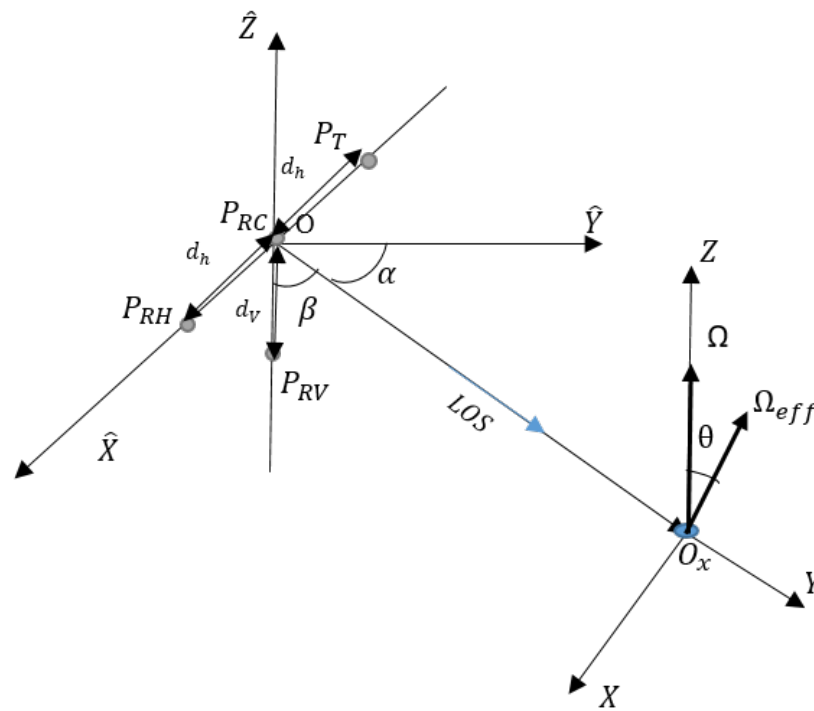


Figure 4. InSAR acquisition geometry.

The target is assumed to be a rigid body consisting of N_t point-like scatterers. The Y -axis is chosen to be the LOS direction. The projection of the rotation vector onto the plan orthogonal to Y defines the effective rotational vector $\Omega_{eff}(t)$. According to [35], the axis X and Y define the imaging plane, (Y corresponds to the range and X to the cross-range). The axis Z is tilted by an angle θ with respect to the effective rotation vector.

The antenna located at the position P_T transmits a wide-band pulse. The signal back-scattered to the n th receiving antenna for a single point scatterer of reflectivity a_n , with time-varying position vector in the T_{XYZ} frame denoted as $\mathbf{x}(t) = [x(t), y(t), z(t)]$ can be written as

$$S_n(f, t) \approx a_n \exp\left(-j\frac{4\pi f}{c}d_{0_n}(t)\right) \exp\left(-j\frac{4\pi f}{c}[\mathbf{x} \cdot (\mathbf{i}_{P_T} + \mathbf{i}_{P_n})]\right) W(f, t) \quad (9)$$

where

$$W(f, t) = \text{rect}\left(\frac{t}{T_{obs}}\right) \cdot \text{rect}\left(\frac{f - f_0}{B}\right) \quad (10)$$

delimitates the frequency and the time domains over which signals are measured, with T_{obs} as the observation time, f_0 as the carrier frequency, and B as the signal bandwidth. The distance $d_{0_n}(t) = (d_{P_T}(t) + d_{P_{R_n}}(t))/2$ accounts for the distances between P_T and the target center O_x and between the P_{R_n} and O_x at time t , where $n \in \{C, V, H\}$ indicates the receiver. Finally, $\mathbf{i}_{P_T}(t)$ is the LOS unit vector of the transmitted antenna, and $\mathbf{i}_{P_{R_n}}(t)$ is the one for a receiving antenna.

As the distance between the system and the target is much larger than the distances separating the antenna, it is assumed that $a_n \approx a$ in the following.

Assuming that $\mathbf{i}_{P_n} = \mathbf{i}_{P_T} + \mathbf{i}_{P_{R_n}}$. The scalar product $\mathbf{x} \cdot \mathbf{i}_{P_n}$ represents the distance between the focusing point O_x and the projection of the scatterer onto the LOS. When the rotational vector is constant during the observation time $\Omega(t) \equiv \Omega(0)$ for $|t| \leq T_{obs}$, the instantaneous displacement vector $\mathbf{x}(t)$ of the scatterer satisfies the differential equation:

$$\frac{\partial \mathbf{x}(t)}{\partial t} = \boldsymbol{\Omega} \times \mathbf{x}(t) \quad (11)$$

Using a first-order Taylor expansion for displacement, the received signal after motion compensation with range alignment is as follows:

$$S_n(f, t) = a \exp\left(-j \frac{4\pi f}{c} [\mathbf{x}_0 \cdot \mathbf{i}_{P_n}]\right) \text{rect}\left(\frac{f - f_0}{B}\right) \exp\left(-j \frac{4\pi f}{c} [(\boldsymbol{\Omega} \times \mathbf{x}_0) \cdot \mathbf{i}_{P_n}] t\right) \text{rect}\left(\frac{t}{T_{obs}}\right) \quad (12)$$

where $\mathbf{x}_0 = \mathbf{x}(t)$ when $t = 0$.

4. 3D Target Reconstruction

4.1. Estimation of the Positions of Scattering Centers

The block diagram for the extraction and 3D localization of the scattering centers of the scene shown in Figure 5 is inspired by the original techniques proposed in [5,18]. Once the received signals have been estimated from the single output of the chaotic cavity, three ISAR images are first reconstructed with the conventional ISAR technique of [5,18].

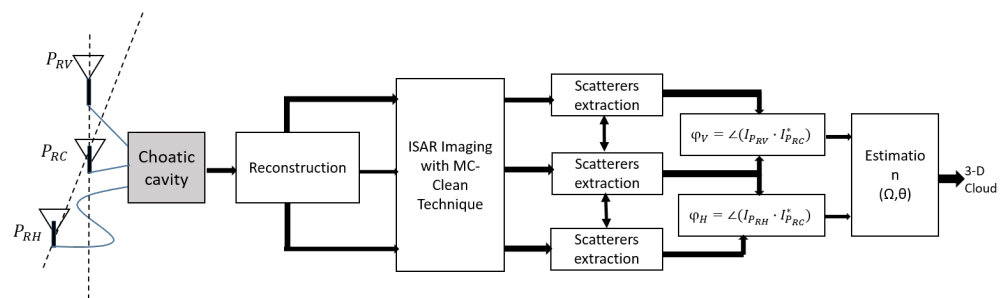


Figure 5. Block diagram of the dual baseline InSAR processing including a hardware compressive coding device.

The MC-Clean [5,18] aims to extract the brightest scattering center in one of the multichannel ISAR images and find its coordinates in the image plane. This algorithm performs an iterative process where the point spread function of the brightest scattering center is estimated and removed from the ISAR images. The algorithm stops when the residual energy in the ISAR image at the k th iteration is lower than a preset threshold, usually set a value significantly higher than the noise ground floor. The phase differences related to the actual elevation and Döppler rate of each scatterers, and to the location of each of the receiving antenna, are measured for the most dominant responses in the observed scene.

$$\begin{aligned} \varphi_V &= \frac{4\pi}{\lambda} (\mathbf{x}_0 \cdot (\mathbf{i}_{P_V} - \mathbf{i}_{P_C})) \\ \varphi_H &= \frac{4\pi}{\lambda} (\mathbf{x}_0 \cdot (\mathbf{i}_{P_H} - \mathbf{i}_{P_C})). \end{aligned} \quad (13)$$

The Doppler frequency is directly related to the cross-range coordinate, which may be expressed after some mathematical manipulations [36] as a function of the phases differences and the incidence angle θ :

$$v_c = -\frac{d_{0c} \Omega_{eff}}{2\pi} \left(\frac{\varphi_H}{d_H} \cos(\theta) + \frac{\varphi_V}{d_V} \sin(\theta) \right) \quad (14)$$

Now, the aspect angle θ and the effective rotation Ω_{eff} can both be estimated from (14) over a common linear regression plan. The components z represents the height of the

scatterer with respect to the image projection plane, and can be approximated as a function of the phase differences and of the angle

$$z \approx \frac{\lambda}{4\pi d_{0c}} \left(\frac{\varphi_V}{d_V} \cos \theta - \frac{\varphi_H}{d_H} \sin \theta \right). \quad (15)$$

where λ is the wavelength and d_H and d_V stand for the effective horizontal and vertical baselines, respectively.

4.2. Baselines Constraints

The upper limits of the vertical and horizontal baselines that guarantee unambiguous phase measurements are given by:

$$d_V \leq \frac{\lambda R_0}{2h_V}, \quad d_H \leq \frac{\lambda R_0}{2h_H} \quad (16)$$

where h_V and h_H are the maximum extent of the observed scatterers positions with respect to the imaging plane in both directions.

4.3. Image Distortion with Squint Mode

For a reconstruction of the InSAR 3D image in a cartesian reference frame T_1 , a correction of the slanted and squinted geometry of the radar acquisition is necessary [37,38]. For a target located at $t = 0$ at the position $(\hat{X}_{0x}, \hat{Y}_{0x}, \hat{Z}_{0x})$ in the frame T_0 , the orientations angles can be expressed as

$$\begin{aligned} \alpha &= \arctan\left(\frac{\hat{X}_{0x}}{\hat{Y}_{0x}}\right) \\ \beta &= \arctan\left(\frac{\hat{Z}_{0x}}{\sqrt{\hat{X}_{0x}^2 + \hat{Y}_{0x}^2}}\right) \end{aligned} \quad (17)$$

Then, the LOS direction for the system can be written as:

$$\mathbf{i}_{LOS} = [\sin \beta \sin \alpha, \sin \beta \cos \alpha, \cos \beta]$$

For any scattering center P of the target, the projection coordinate of a point P onto the reference system T_1 is:

$$\mathbf{r} = \mathbf{O}_x \mathbf{P} \cdot \mathbf{i}_{LOS} = \begin{bmatrix} x \sin \beta \sin \alpha \\ y \sin \beta \cos \alpha \\ z \cos \beta \end{bmatrix} \quad (18)$$

Distortions of the original image geometry are due to the fact that the coordinates P are defined in the slant range, as shown in (18). Setting $\beta = \pi/2$ and $\alpha = 0$, transforms the slant range axis R into the ground the range axis Y , which corresponds to the standard reference configuration.

5. Simulation Results

The proposed approach is validated using a simulation performed according to the configuration shown in Figure 6. A rigid body mimicking the shape of an airplane composed of $M = 10$ metallic scatterers is considered. The target moves on a straight line, defined by roll, pitch and yaw angles, with respect to the radar Line Of Sight (LOS), with a speed of 8 m/s. The parameters used numerically are shown in Table 1. The geometry of the target in X-Y-Z cartesian coordinates is displayed in Figure 7.

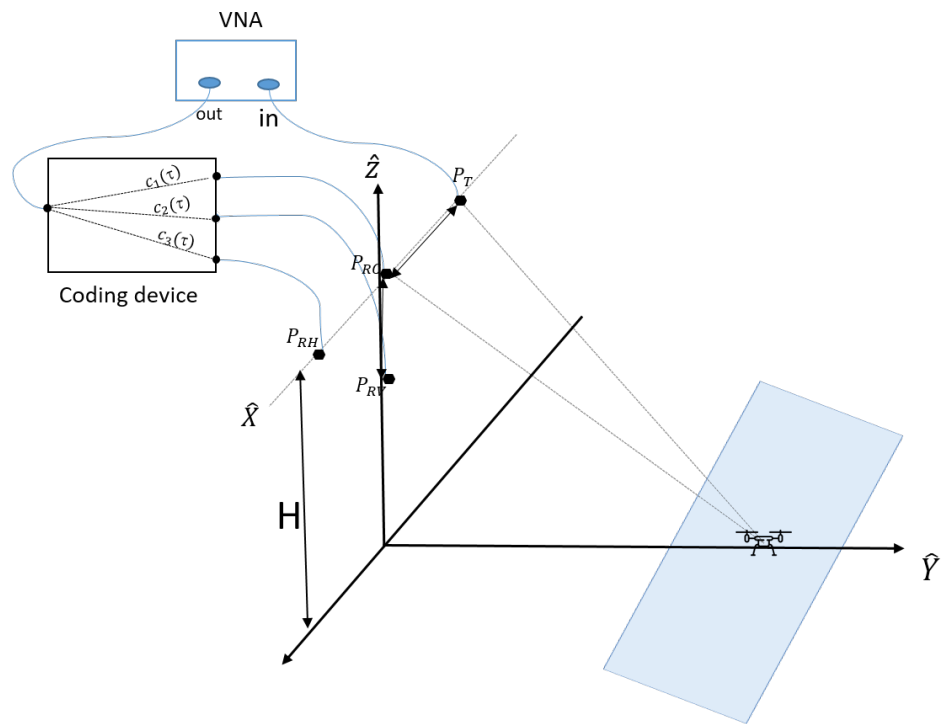


Figure 6. Simulated configuration including a hardware coding device connection and an antenna array.

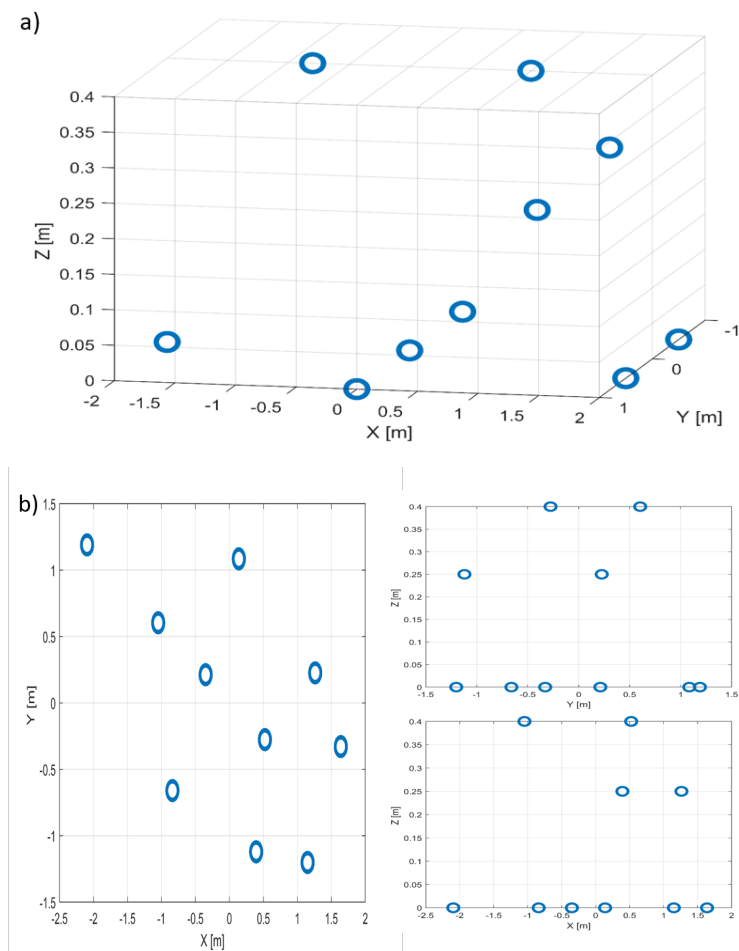


Figure 7. Simulated object description. (a) 3D. (b) Top, side and front views.

Table 1. Radar acquisition parameters.

Parameters	Values
Carrier frequency	6 GHz
Signal bandwidth	2 GHz
Baseline ($d_h = d_v$)	30 cm
Number of frequency samples	2001
Number of radar sweeps	120
PRF	800 Hz
Ground range	25.5 m
Roll/Pitch/Yaw	0° 0° 60°
Radar height	5 m

The simulation of the response of the imaged set of scatterers is performed using advanced inverse techniques [39,40] in the case of a classical multi-channel system. Hardware compressed signals are then obtained by applying the chaotic cavity transfer function, measured experimentally, onto the simulated signals. Focusing results obtained using the Range–Doppler algorithm are shown in Figure 8, and indicate that the 2D imaging resolution is not deteriorated by the use of the hardware multiplexer. However, strong side lobes appear when the compressive device is used, as illustrated in Figure 9. These side lobes are inherent of the inversion procedure [31] and obviously limit the dynamic range of the reconstructed image.

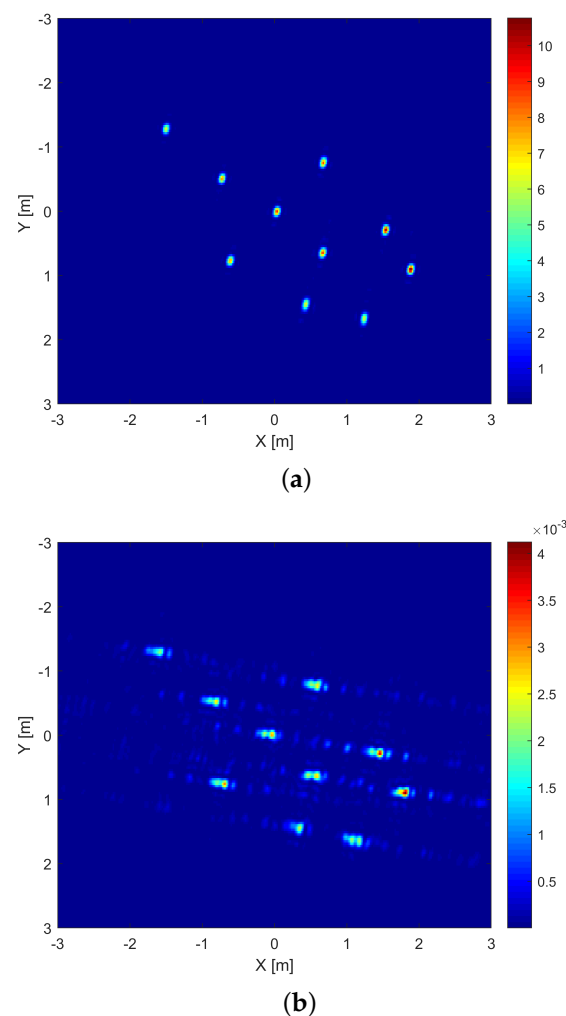


Figure 8. Two–dimensional images of a single channel after motion compensation of the simulated scene response. (a) measured by an antenna; (b) reconstructed from the output signal of the chaotic cavity.

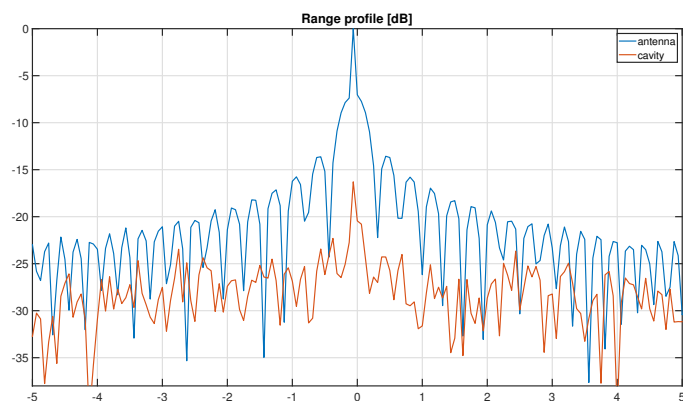


Figure 9. Normalized azimuth slice of the ISAR image of a single scatterer response.

The 3D reconstruction of the scattering center position obtained with the Clean Technique is shown in Figure 10. The application of MC-Clean allows us to limit the influence of sidelobes induced by the reconstruction of the signals from the output of the chaotic cavity. Slight offsets on the location of the scatterers are, however, found in both cases, due to the approximations associated with the compensation of 2D uniform target rotation. The reconstruction is slightly deteriorated in the case of the compressive device, as the InSAR algorithm is sensitive to a reduced signal-to-noise ratio, as demonstrated in [5].

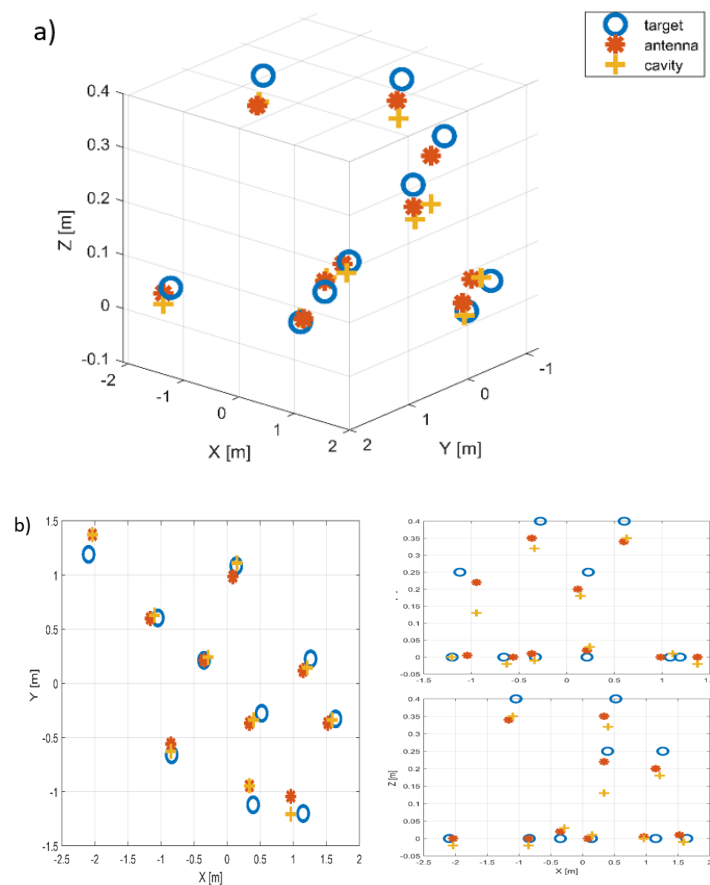


Figure 10. Reconstruction result: (a) 3D, (b) X-Y, X-Z and Y-Z planes. Blue circles represent true scatterer locations, red stars indicate those estimated using a multi-channel system, and yellow crosses represent results obtained using the chaotic cavity.

6. Experimental Result

An experiment was carried out using hardware and software facilities developed for 3D Ground-Based SAR campaigns dedicated to the refined characterization of volumetric environments [41–44]. The geometrical configuration was similar to the one used to simulate signals, but with a reference antenna P_C located at a height of 5.5 m above the ground, and at ground range distance of 5.5 m from the center of the scene. The target composed of three trihedral reflectors—see Table 2—translated on a 3 m-long rail lying on the ground, with a step length of $\lambda/4 \sim 9$ mm with an orientation of 60° . Measurements were first performed with a multi-port VNA connected to the antenna system, and then using the chaotic cavity and a single port.

Table 2. Trihedral reflector positions with respect to the target center.

Trihedral Number	(X, Y, Z)
1	(0, 0, 0)
2	(0.5, 0, 0)
3	(0, 0.3, 0.35)

After compensation of the target trajectory, the RD algorithm was applied to the data measured by each antenna and after reconstruction with the compressive device. The ISAR images in range and cross-range coordinates are shown in Figure 11 and confirm that the use of a chaotic compressive hardware device induce stronger side lobes and affects the quality of the ISAR image. In this context, the Clean technique, which is able to extract the complete impulse response from the total signal, is very important, as high sidelobes may mask low-reflectivity scatterers.

Among a full dataset, a subset of data corresponding to the third of path was chosen for analysis (Figure 12), as it appears to limit migration in distance. Therefore, each scatterer must have the same range-azimuth coordinates for all three images. The MC-Clean technique was applied to the data with a threshold of 10% from the strongest peak image in the ISAR images for both measurements. A total of three scatterers was extracted for each measurement. The Figure 13 shows the estimated 3D cloud point in red for MC-clean with antennas, in yellow for MC-Clean after reconstruction, aligned with the model in blue.

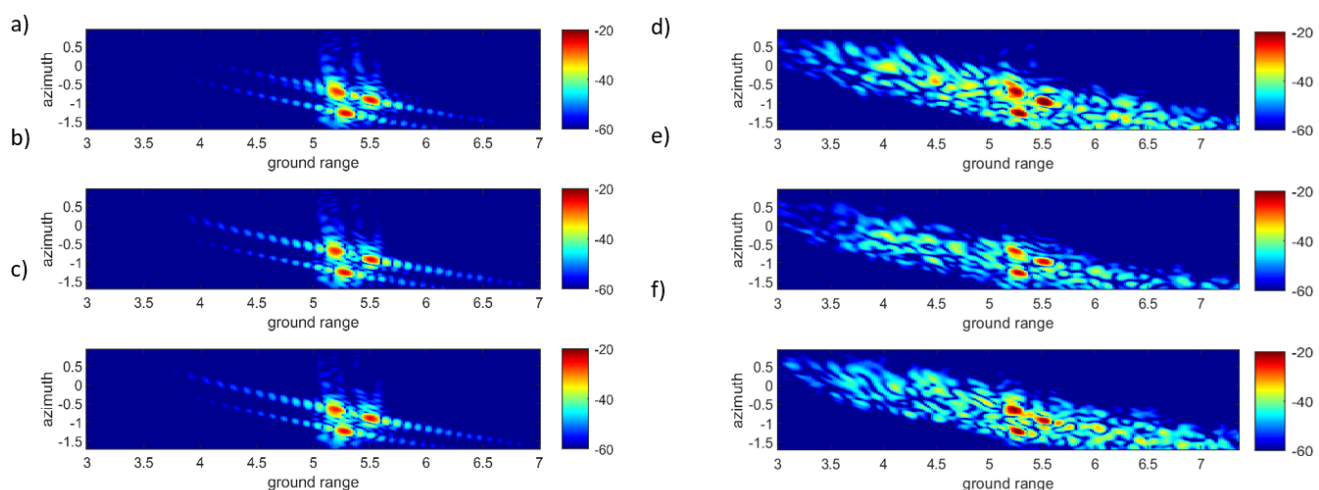


Figure 11. 2–D images normalized obtained after motion compensation the signals on the three receivers antennas: measurement with antennas (a) P_C . (b) P_H . (c) P_V , with cavity after reconstruction: (d) P_C . (e) P_H . (f) P_V .

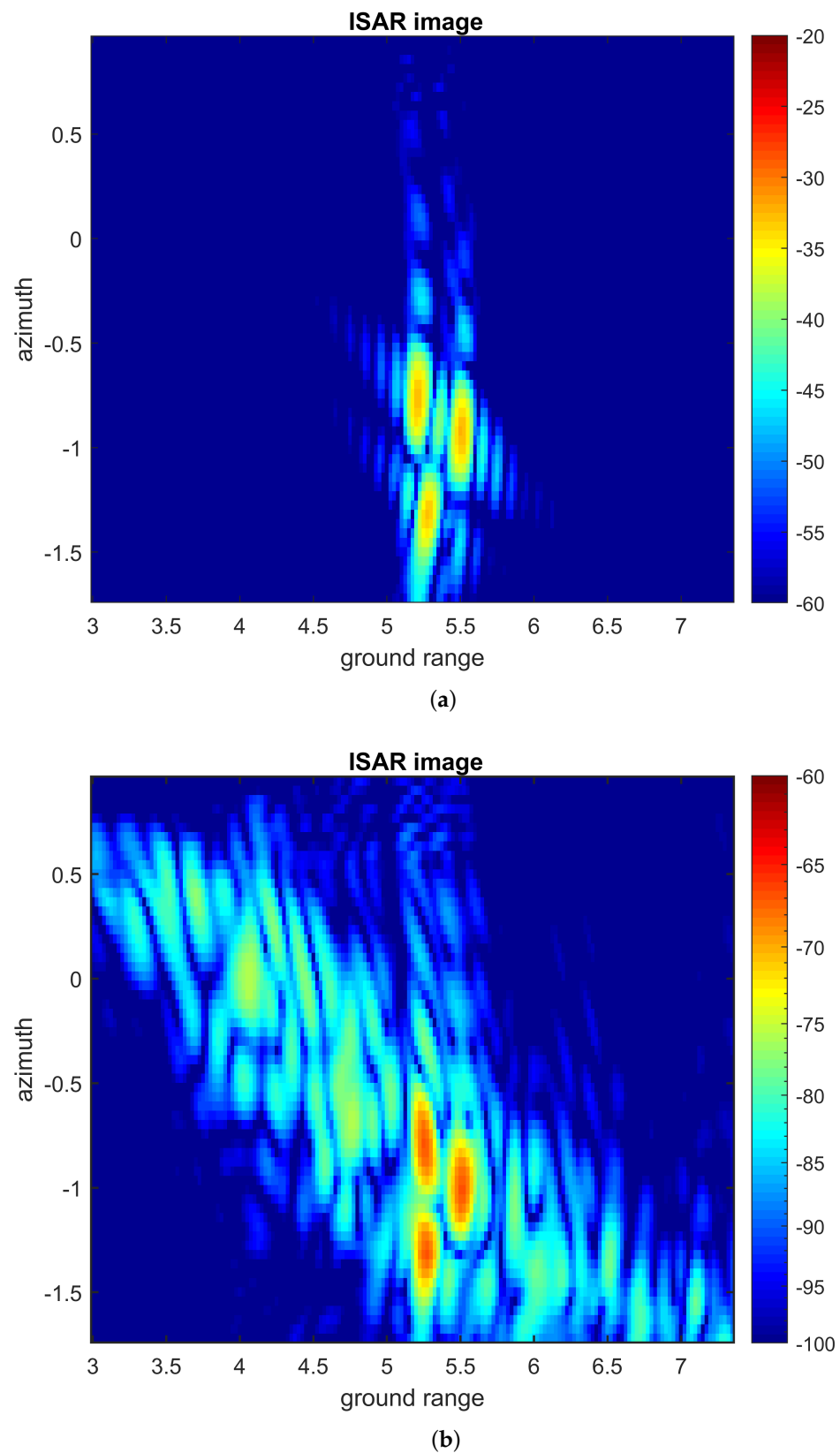


Figure 12. Two-dimensional images after motion compensation: (a) measurement with antennas P_C . (b) with cavity after reconstruction.

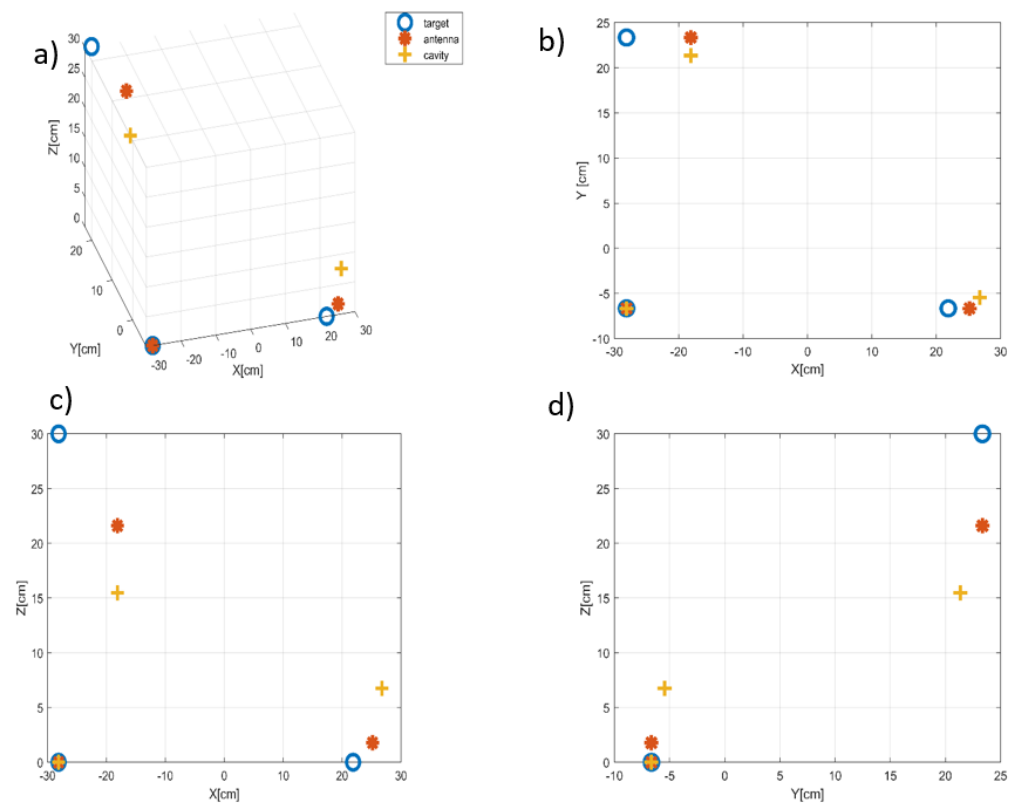


Figure 13. Scatterers positions retrieved using experimental data acquired with and without the cavity. (a) 3D, (b) top, (c) side, (d) front views.

The reconstruction operated using multiple receiving channels led to an RMS error of $\zeta = 9$ cm, whereas the one obtained with the compressive device was $\zeta = 17$ cm. Estimated target dimensions, whose calculation is a key aspect of InISAR, are given in Table 3. These results are in agreement with the actual target values. However, there are several factors that influence the results on the real data, such as the estimated position of the scene center and the phase difference between the antennas. A perfect trajectory compensation allows us to limit the errors of the Doppler measurement. The residual correlation between the transfer functions of the chaotic cavity may be considered as a source of error, too, as it affects the quality of phase calculation and Doppler measurement.

Table 3. True and estimated target dimension.

Measurement	Length (cm)	Width (cm)	Height (cm)
True value	50	30	35
Multichannel InISAR	52	29	21
Single compressed channel	55	28	15

7. Conclusions

This paper proposes using a compressive device to reduce the complexity of an InISAR technique, which requires us to simultaneously measure signals at different antenna positions. The objective is to minimize the complexity of the acquisition system and still benefit from the robustness and simplicity of the InISAR 3D-focusing approach for a scaled reconstruction of a complex moving target. Simulations show that the hardware compressive device considered in this study, a chaotic cavity, does not affect the imaging resolution, but involves the presence of side lobes which may affect the characterization of complex targets. Nevertheless, the iterative estimation approach used in the InISAR

method reaches good performance, as it subtracts the entire impulse of a scatterer from the total signal, i.e., it can handle sidelobes efficiently. Experimental results, obtained with a three-element L-shaped antenna array connected to a metallic enclosure, led to a reconstruction in very good agreement with true scatterer positions. Hence, this study demonstrates that compressive approaches represent a promising and low-cost solution to overcome synchronisation problems for acquisition of configurations involving several receiving channels.

Author Contributions: Conceptualization, methodology, software, validation, M.D.L., M.D. and L.F.-F.; formal analysis, L.F.-F. and M.D.L.; investigation, resources, data curation, writing—original draft preparation M.D.L. and M.D.; writing—review and editing, M.D.L., M.D. and L.F.-F.; supervision, M.D. and L.F.-F. All authors have read and agreed to the published version of the manuscript.

Funding: This research was funded by the European Regional Development Fund (ERDF) and French region of Brittany and Rennes Métropole through the CPER Project SOPHIE/STIC & Ondes.

Data Availability Statement: Not applicable.

Conflicts of Interest: The authors declare no conflict of interest.

References

1. Chen, V.C.; Martorella, M. *Inverse Synthetic Aperture Radar Imaging: Principles, Algorithms and Applications*; Institution of Engineering and Technology: Stevenage, UK, 2014.
2. Pastina, D.; Spina, C. Multi-feature based automatic recognition of ship targets in ISAR. *Sonar Navig. IET Radar* **2009**, *3*, 406–423. [[CrossRef](#)]
3. Leducq, P.; Ferro-Famil, L.; Pottier, E. Matching-Pursuit-Based Analysis of Moving Objects in Polarimetric SAR Images. *IEEE Geosci. Remote Sens. Lett.* **2008**, *5*, 123–127. [[CrossRef](#)]
4. Hu, C.; Ferro-Famil, L.; Kuang, G. Ship discrimination using polarimetric SAR data and coherent time-frequency analysis. *Remote Sens.* **2013**, *5*, 6899–6920. [[CrossRef](#)]
5. Martorella, M.; Stagliano, D.; Salvetti, F.; Battisti, N. 3D interferometric ISAR imaging of noncooperative targets. *IEEE Trans. Aerosp. Electron. Syst.* **2014**, *50*, 3102–3114. [[CrossRef](#)]
6. Cooke, T. Scatterer labelling estimation for 3D model reconstruction from an ISAR image sequence. In Proceedings of the 2003 Proceedings of the International Conference on Radar (IEEE Cat. No.03EX695), Adelaide, Australia, 3–5 September 2003; pp. 315–320. [[CrossRef](#)]
7. Cooke, T. Ship 3D model estimation from an ISAR image sequence. In Proceedings of the 2003 International Conference on Radar (IEEE Cat. No.03EX695), Adelaide, Australia, 3–5 September 2003; pp. 36–41. [[CrossRef](#)]
8. Mayhan, J.; Burrows, M.; Cuomo, K.; Piou, J. High resolution 3D “snapshot” ISAR imaging and feature extraction. *Aerosp. Electron. Syst. IEEE Trans.* **2001**, *37*, 630–642. [[CrossRef](#)]
9. Knaell, K.K.; Cardillo, G. Radar tomography for the generation of three-dimensional images. *IEEE Proc.-Radar Sonar Navig.* **1995**, *142*, 54–60. [[CrossRef](#)]
10. Zhou, C.; Jiang, L.; Yang, Q.; Ren, X.; Wang, Z. High Precision Cross-Range Scaling and 3D Geometry Reconstruction of ISAR Targets Based on Geometrical Analysis. *IEEE Access* **2020**, *8*, 132415–132423. [[CrossRef](#)]
11. Liu, L.; Zhou, F.; Bai, X.; Tao, M.; Zhang, Z.J. Joint Cross-Range Scaling and 3D Geometry Reconstruction of ISAR Targets Based on Factorization Method. *IEEE Trans. Image Process.* **2016**, *25*, 1740–1750. [[CrossRef](#)]
12. Wang, F.; Xu, F.; Jin, Y. 3-D information of a space target retrieved from a sequence of high-resolution 2-D ISAR images. In Proceedings of the 2016 IEEE International Geoscience and Remote Sensing Symposium (IGARSS), Beijing, China, 10–15 July 2016; pp. 5000–5002.
13. Jiao, Z.; Ding, C.; Chen, L.; Zhang, F. Three-Dimensional Imaging Method for Array ISAR Based on Sparse Bayesian Inference. *Sensors* **2018**, *18*, 3563. [[CrossRef](#)]
14. Wang, G.; Xia, X.G.; Chen, V. Three-dimensional ISAR imaging of maneuvering targets using three receivers. *IEEE Trans. Image Process.* **2001**, *10*, 436–447. [[CrossRef](#)]
15. Given, J.; Schmidt, W. Generalized ISAR-part II: Interferometric techniques for three-dimensional location of scatterers. *IEEE Trans. Image Process.* **2005**, *14*, 1792–1797. [[CrossRef](#)]
16. Battisti, N.; Martorella, M. Interferometric phase and target motion estimation for accurate 3D reflectivity reconstruction in ISAR systems. In Proceedings of the 2010 IEEE Radar Conference, Arlington, VA, USA, 10–14 May 2010; pp. 108–112. [[CrossRef](#)]
17. Xu, X.; Luo, H.; Huang, P. 3-D interferometric ISAR images for scattering diagnosis of complex radar targets. In Proceedings of the 1999 IEEE Radar Conference—Radar into the Next Millennium (Cat. No.99CH36249), Waltham, MA, USA, 22 April 1999; pp. 237–241. [[CrossRef](#)]

18. Staglianò, D.; Lischi, S.; Massini, R.; Musetti, L.; Martorella, M.; Berizzi, F. Soft 3D-ISAR image reconstruction using a dual interferometric radar. In Proceedings of the 2015 IEEE Radar Conference (RadarCon), Arlington, VA, USA, 10–15 May 2015; pp. 0572–0576. [\[CrossRef\]](#)
19. Xu, X.; Narayanan, R. Three-dimensional interferometric ISAR imaging for target scattering diagnosis and modeling. *IEEE Trans. Image Process.* **2001**, *10*, 1094–1102. [\[CrossRef\]](#) [\[PubMed\]](#)
20. Fontana, A.; Berens, P.; Staglianò, D.; Martorella, M. 3D ISAR/SAR imaging using multichannel real data. In Proceedings of the 2016 IEEE Radar Conference (RadarConf), Philadelphia, PA, USA, 2–6 May 2016; pp. 1–4.
21. Zheng, J.; Liu, H.; Liu, Z.; Liu, Q.H. ISAR Imaging of Ship Targets Based on an Integrated Cubic Phase Bilinear Autocorrelation Function. *Sensors* **2017**, *17*, 498. [\[CrossRef\]](#) [\[PubMed\]](#)
22. Zhao, L.; Gao, M.; Martorella, M.; Stagliano, D. Bistatic three-dimensional interferometric ISAR image reconstruction. *IEEE Trans. Aerosp. Electron. Syst.* **2015**, *51*, 951–961. [\[CrossRef\]](#)
23. Staglianò, D.; Martorella, M.; Casalini, E. Interferometric bistatic ISAR processing for 3D target reconstruction. In Proceedings of the 2014 11th European Radar Conference, Rome, Italy, 8–10 October 2014; pp. 161–164. [\[CrossRef\]](#)
24. Yoya, A.C.T.; Fuchs, B.; Leconte, C.; Davy, M. A Reconfigurable Chaotic Cavity with Fluorescent LAMPS for Microwave Computational Imaging. *arXiv* **2018**, arXiv:1810.07099.
25. Yoya, A.C.T.; Fuchs, B.; Davy, M. Computational passive imaging of thermal sources with a leaky chaotic cavity. *Appl. Phys. Lett.* **2017**, *111*, 193501. [\[CrossRef\]](#)
26. Fromenteze, T.; Kpré, E.L.; Carsenat, D.; Decroze, C. CLEAN Deconvolution Applied to Passive Compressed Beamforming. *Prog. Electromagn. Res.* **2015**, *56*, 163–172. [\[CrossRef\]](#)
27. Manzacca, G.; Paciotti, D.; Marchese, A.; Moreolo, M.S.; Cincotti, G. 2D photonic crystal cavity-based WDM multiplexer. *Photonics Nanostruct. Fundam. Appl.* **2007**, *5*, 164–170. [\[CrossRef\]](#)
28. Davy, M.; Fink, M.; de Rosny, J. Green's Function Retrieval and Passive Imaging from Correlations of Wideband Thermal Radiations. *Phys. Rev. Lett.* **2013**, *110*, 203901. [\[CrossRef\]](#)
29. Liutkus, A.; Martina, D.; Popoff, S.; Chardon, G.; Katz, O.; Lerosey, G.; Gigan, S.; Daudet, L.; Carron, I. Imaging with Nature: Compressive Imaging Using a Multiply Scattering Medium. *Sci. Rep.* **2014**, *4*, 5552. [\[CrossRef\]](#)
30. Fromenteze, T.; Kpré, E.L.; Decroze, C.; Carsenat, D.; Yurduseven, O.; Imani, M.; Gollub, J.; Smith, D.R. Unification of compressed imaging techniques in the microwave range and deconvolution strategy. In Proceedings of the 2015 European Radar Conference (EuRAD), Paris, France, 9–11 September 2015.
31. Fromenteze, T.; Yurduseven, O.; Imani, M.F.; Gollub, J.; Decroze, C.; Carsenat, D.; Smith, D.R. Computational imaging using a mode-mixing cavity at microwave frequencies. *Appl. Phys. Lett.* **2015**, *106*, 194104. [\[CrossRef\]](#)
32. Jouadé, A.; Meric, S.; Lafond, O.; Himdi, M.; Ferro Famil, L. A Passive Compressive Device Associated with a Luneburg Lens for Multi-beam Radar at Millimeter-wave. *IEEE Antennas Wirel. Propag. Lett.* **2018**, *17*, 938–941. [\[CrossRef\]](#)
33. Jouade, A.; Lafond, O.; Ferro-Famil, L.; Himdi, M.; Méric, S. Passive Compressive Device in an MIMO Configuration at Millimeter Waves. *IEEE Trans. Antennas Propag.* **2018**, *66*, 5558–5568. [\[CrossRef\]](#)
34. Tian, B.; Zhejun, L.; Liu, Y.; Li, X. Review on Interferometric ISAR 3D Imaging: Concept, Technology and Experiment. *Signal Process.* **2018**, *153*, 164–187. [\[CrossRef\]](#)
35. Walker, J.L. Range-Doppler Imaging of Rotating Objects. *IEEE Trans. Aerosp. Electron. Syst.* **1980**, *AES-16*, 23–52. [\[CrossRef\]](#)
36. Benedek, C.; Martorella, M. Moving Target Analysis in ISAR Image Sequences With a Multiframe Marked Point Process Model. *IEEE Trans. Geosci. Remote Sens.* **2014**, *52*, 2234–2246. [\[CrossRef\]](#)
37. Tian, B.; Zou, J.; Chen, Z.; Shiyu, X. Squint model interferometric ISAR imaging based on respective reference range selection and squint iteration improvement. *IET Radar Sonar Navig.* **2015**, *9*, 1366–1375. [\[CrossRef\]](#)
38. Tian, B.; Liu, Y.; Tang, D.; Xu, S.; Chen, Z. Interferometric ISAR imaging for space moving targets on a squint model using two antennas. *J. Electromagn. Waves Appl.* **2014**, *28*, 2135–2152. [\[CrossRef\]](#)
39. Khwaja, S.A.; Ferro-Famil, L.; Pottier, E. Efficient SAR Raw Data Generation for Anisotropic Urban Scenes Based on Inverse. *IEEE Geosci. Remote Sens. Lett.* **2009**, *6*, 757–761. [\[CrossRef\]](#)
40. Khwaja, S.A.; Ferro-Famil, L.; Pottier, E. Efficient Stripmap SAR Raw Data Generation Taking Into Account Sensor Trajectory Deviations. *IEEE Geosci. Remote Sens. Lett.* **2011**, *8*, 794–798. [\[CrossRef\]](#)
41. Rekioua, B.; Davy, M.; Ferro-Famil, L.; Tebaldini, S. Snowpack permittivity profile retrieval from tomographic SAR data. *C. R. Phys.* **2017**, *18*, 57–65. [\[CrossRef\]](#)
42. Yitayew, T.G.; Ferro-Famil, L.; Eltoft, T.; Tebaldini, S. Tomographic Imaging of Fjord Ice Using a Very High Resolution Ground-Based SAR System. *IEEE Trans. Geosci. Remote Sens.* **2017**, *55*, 698–714. [\[CrossRef\]](#)
43. Yitayew, T.G.; Ferro-Famil, L.; Eltoft, T.; Tebaldini, S. Lake and Fjord Ice Imaging Using a Multifrequency Ground-Based Tomographic SAR System. *IEEE J. Sel. Top. Appl. Earth Obs. Remote Sens.* **2017**, *10*, 4457–4468. [\[CrossRef\]](#)
44. Harkati, L.; Abdo, R.; Avrillon, S.; Ferro-Famil, L. Low Complexity Portable MIMO Radar System for the Characterization of Complex Environments at High Resolution. *IET Radar Sonar Navig.* **2020**, *14*, 992–1000. [\[CrossRef\]](#)